Quantum-optical coherence tomography with collinear entangled photons

Dorilian Lopez-Mago[1,2] and Lukas Novotny[1,2,3,*]

[1]*Institute of Optics, University of Rochester, Rochester, New York 14627, USA*

[2]*Photonics and Mathematical Optics Group, Tecnológico de Monterrey, Monterrey, Nuevo León 64849, Mexico*

[3]*ETH Zürich, Photonics Laboratory, 8093 Zürich, Switzerland*

**Corresponding author: novotny@optics.rochester.edu*

Received July 31, 2012; accepted August 10, 2012;
posted August 21, 2012 (Doc. ID 173583); published September 25, 2012

Quantum-optical coherence tomography (QOCT) combines the principles of classical OCT with the correlation properties of entangled photon pairs [Phys. Rev. A **65**, 053817 (2002)]. The standard QOCT configuration is based on the Hong–Ou–Mandel interferometer, which uses entangled photons propagating in separate interferometer arms. This noncollinear configuration imposes practical limitations, e.g., misalignment due to drift and low signal-to-noise. Here, we introduce and implement QOCT based on *collinear* entangled photons. It makes use of a two-photon Michelson interferometer and offers several advantages, such as simplicity, robustness, and adaptability.

OCIS codes: 270.1670, 270.4180, 270.5290.

Quantum-optical coherence tomography (QOCT) uses a Hong–Ou–Mandel (HOM) interferometer to record tomographic images of a reflective sample [1]. It makes use of frequency-entangled photon pairs produced by the nonlinear process of spontaneous parametric down-conversion (SPDC). Because the down-converted photons are frequency correlated, QOCT yields dispersion-free measurements and provides enhanced resolution.

The viability of QOCT was experimentally demonstrated by Nasr *et al.* [2]. Later, QOCT was implemented in dispersive media [3], biological samples [4], and polarization-sensitive reflective surfaces [5]. It has been shown that the unique properties of QOCT can be mimicked by phase-conjugate OCT and chirped-pulse OCT, which offer enhanced sensitivity and a faster acquisition rate [6,7].

Although the potential applications of QOCT have attracted much attention, current implementations of QOCT face several challenges. First, the noncollinear geometry complicates alignment and the balancing of the interferometer arms. Second, the need of selecting a small angular range from the down-converted emission cone drastically reduces the flux of down-converted photon pairs.

In this Letter we demonstrate the implementation of QOCT with *collinear* down-converted photon pairs [8]. We use a Michelson interferometer combined with a coincidence detector and show that by Fourier processing the recorded fourth-order interferogram, we can obtain the same information that is available using the HOM interferometer, but with the benefit of a significantly larger signal.

A schematic of the standard HOM configuration is shown in Fig. 1(a). A quasi-monochromatic laser of angular frequency ω_p pumps a nonlinear crystal (NLC). A pump photon is spontaneously split into a pair of down-converted photons. The NLC is cut and oriented such that it produces type I SPDC with both photons having the same polarization and center frequency $\omega_0 = \omega_p/2$. One of the photons is directed to the sample and the other photon to a controllable temporal delay τ. After the two photons scatter and reflect from the sample and the delay stage, respectively, they are recombined at a beam splitter. At the output ports, two photodetectors measure the coincidence count rate $C(\tau)$. The coincidence count rate yields a dip when the optical path lengths of the two photons are equal (the so-called HOM dip). The dip is a consequence of destructive quantum interference and is used to reconstruct the internal structure of the sample.

The down-converted photons are defined by the joint state $|\psi\rangle = \int \mathrm{d}\,\Omega\,\zeta(\Omega)|\omega_0 + \Omega, \omega_0 - \Omega\rangle$, where Ω represents a frequency shift from ω_0 [1]. $\zeta(\Omega)$ is the joint spectral probability amplitude. The joint spectral density $S(\Omega) = |\zeta(\Omega)|^2$ is a symmetric function and is normalized such that $\int \mathrm{d}\,\Omega\,S(\Omega) = 1$.

The coincidence rate assumes the form $C(\tau) \propto \Lambda_0 - \mathrm{Re}\{\Lambda(2\tau)\}$, where Λ_0 and Λ are self-interference and cross-interference terms, respectively, defined as [1]

$$\Lambda_0 = \int \mathrm{d}\,\Omega |H(\omega_0 + \Omega)|^2 S(\Omega), \tag{1}$$

$$\Lambda(\tau) = \int \mathrm{d}\,\Omega\, H(\omega_0 + \Omega) H^*(\omega_0 - \Omega) S(\Omega) e^{i\Omega\tau}. \tag{2}$$

Here, $H(\omega)$ is the transfer function of the sample. An example of $C(\tau)$ is given in Fig. 1(b). The dips are produced

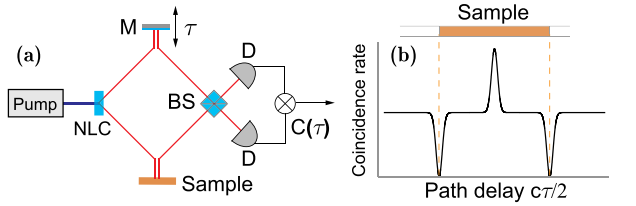

Fig. 1. (Color online) (a) Standard configuration of QOCT based on a HOM interferometer. A laser pumps a nonlinear crystal (NLC) to generate noncollinear entangled photon pairs. The mirror (M) is translated and the coincidences $C(\tau)$ are monitored. (b) Example of a coincidence interferogram. D, detector; BS, beam splitter; τ, time delay.

by destructive quantum interference from reflections from two consecutive interfaces. The peak between the dips arises from the interference between both reflections. It depends on the values of ω_p, the refractive index n between the interfaces, the interface separation L, and the reflection coefficients r_i of each interface. Notice that the peak between the dips depends on a phase factor, which in turn depends on the values of ω_p, n, L, and r_i. The peak can change to a dip, depending on the phase factor. The factor of two in the cross-interference term Λ in $C(\tau)$ is a consequence of entanglement and gives rise to a resolution enhancement compared to conventional OCT. The width of the dips is determined by the product $H(\omega_0+\Omega)H^*(\omega_0-\Omega)$. Because of frequency-entanglement, the width is immune to even-order dispersion.

We now turn our attention to the two-photon Michelson configuration shown in Fig. 2(a). As before, we generate type I down-converted photons, but now with the phase-matching condition arranged such that the down-converted photons propagate collinearly. This situation corresponds to the spatially degenerate case of SPDC. As shown in Fig. 2(b), there are four possibilities for the down-converted photons to propagate through the interferometer. Both photons can be transmitted/reflected and then reflected/transmitted [cases (i) and (ii)], or one is transmitted while the other is reflected [cases (iii) and (iv)]. The superposition of the four probability amplitudes produces the coincidence rate

$$M(\tau) \propto M_0 + 2\,\mathrm{Re}\{M_1(2\tau)\} + 4\,\mathrm{Re}\{M_2(\tau)e^{-i\omega_0\tau}\} + 2\,\mathrm{Re}\{M_3 e^{-i2\omega_0\tau}\}, \tag{3}$$

with the interference factors M_i given by

$$M_0 = \int \mathrm{d}\,\Omega\,(1+|H(\omega_0-\Omega)|^2)(1+|H(\omega_0+\Omega)|^2)S(\Omega), \tag{4}$$

$$M_1(\tau) = \int \mathrm{d}\,\Omega\,H(\omega_0+\Omega)\,H^*(\omega_0-\Omega)S(\Omega)e^{i\Omega\tau}, \tag{5}$$

$$M_2(\tau) = \int \mathrm{d}\,\Omega\,(1+|H(\omega_0-\Omega)|^2)\;\;H(\omega_0+\Omega)S(\Omega)e^{-i\Omega\tau}, \tag{6}$$

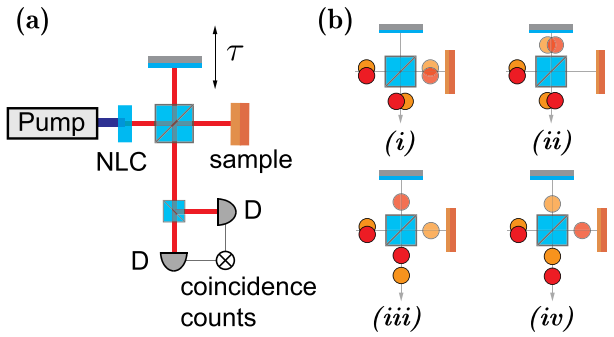

Fig. 2. (Color online) (a) Implementation of QOCT with the two-photon Michelson interferometer. (b) Illustration of the four possibilities of pairwise photon propagation through the interferometer.

$$M_3 = \int \mathrm{d}\,\Omega\,H(\omega_0+\Omega)H(\omega_0-\Omega)S(\Omega). \tag{7}$$

The self-interference factor M_0 corresponds to the average number of coincidences and is equivalent to Λ_0 in Eq. (1). The cases (iii) and (iv) produce the cross-interference factors M_1 and M_2. The factor M_1 is produced by photon bunching, in the same way as Λ in Eq. (2). M_2 is the classical fourth-order interference between cases (iii) and (iv), which gives rise to interference fringes oscillating with frequency ω_0 [third term in Eq. (3)]. Finally, the term M_3 is produced by the interference of cases (i) and (ii), which corresponds to both photons traveling in pairs through the interferometer. Because of entanglement, the interference of cases (i) and (ii) gives rise to fringes oscillating at $2\omega_0$, which is represented by the last term in Eq. (3).

To use the Michelson interferometer for QOCT we need to isolate the M_1 term, which is equivalent to Λ in Eq. (2), from the other terms in Eq. (3). Because the different terms are spectrally separated, we can numerically isolate $2\,\mathrm{Re}\{M_1(2\tau)\}$ by low-pass filtering. Thus, the two-photon Michelson interferometer provides the same information as the HOM interferometer, but with the advantage of a collinear arrangement.

To validate the theoretical predictions we have set up a two-photon Michelson interferometer using a 100 mW diode laser with nominal wavelength of 407 nm. The laser pumps a BBO nonlinear crystal whose optical axis is oriented at 3.6 deg with respect to the propagation direction of the laser. This configuration produces type I parametric down-conversion with photon pairs that are emitted collinearly with a center wavelength of 814 nm. After the crystal, the pump laser is rejected with a combination of a polarizing beam splitter and a longpass filter. The down-converted photons are directed into the Michelson interferometer and the output is analyzed by means of coincidence detection.

To further suppress the pump laser we use bandpass filters in front of the detectors. The filters have a bandwidth of 10 nm centered at 810 nm. Because the bandwidth of the filters is smaller than the bandwidth of the down-converted photons, the joint spectral density $S(\Omega)$ can be approximated by the transmissivity F of the filters, that is, $S(\Omega) \approx F(\Omega)$. Note that the bandpass filters reduce the image resolution and the flux of down-converted photons. However, their use is not a requirement and they can be replaced by polarizers with higher extinction ratio.

As a test sample we use a glass cover slip with a thickness of about 110 μm. A 10 nm gold film has been deposited on either side of the cover slip. An interferogram is recorded by translating the reference mirror and monitoring the coincidence count rate. The raw interferogram is shown in Fig. 3(a), and the low-pass filtered interferogram is depicted in Fig. 3(b).

The filtered interferogram features three characteristic peaks. The two outer ones are associated with the location of the surfaces, while the center one originates from the interference between the two surfaces, equivalent to the case of the HOM interferometer discussed earlier. The distance between the outer peaks determines the thickness L of the sample. The measured optical thickness is

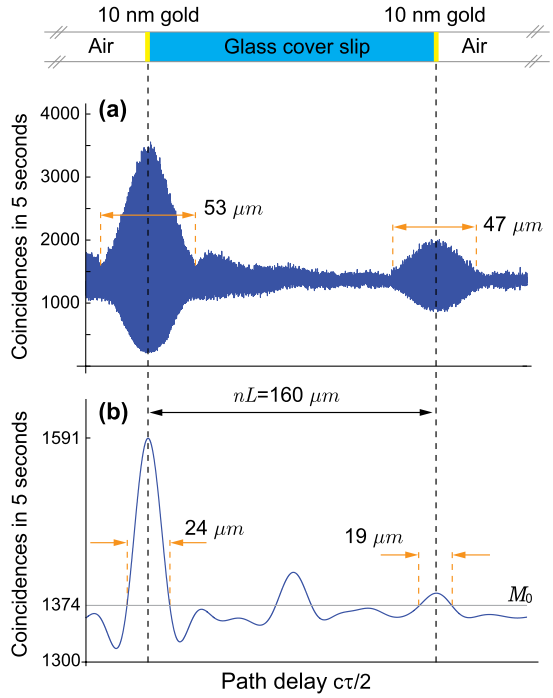

Fig. 3. (Color online) Experimental two-photon interferograms recorded with the Michelson interferometer. The sample consists of two partially reflecting interfaces separated by 110 nm. (a) Recorded coincidence rate $M(\tau)$. (b) Resulting interferogram after low-pass filtering $M(\tau)$. The illustration on the top depicts the sample consisting of two gold coated glass surfaces.

$nL = 160$ μm. Using a glass refractive index of $n = 1.5$ yields a thickness of $L = 106$ μm. Note that each interface gives rise to a sinc function which originates from the bandpass filters. The sinc function is characterized by a center peak and several side lobes, which can be suppressed by numerical deconvolution of the low-pass filtered data. Compared to classical OCT, the two-photon Michelson interferometer yields narrower peaks and hence better resolution.

To demonstrate the spectral separation of the different terms in the interferogram $M(\tau)$ defined in Eq. (3), we Fourier transform the raw data shown in Fig. 3(a). The magnitude of this Fourier transform is rendered in Fig. 4. We have subtracted the average coincidence rate M_0, which gives rise to a delta function at $\omega = 0$. The Fourier transformed data clearly shows the spectral separation of the terms $2\,\mathrm{Re}\{M_1(2\tau)\}$, $4\,\mathrm{Re}\{M_2(\tau)\exp(-i\omega_0\tau)\}$ and $2\,\mathrm{Re}\{M_3\exp(-i2\omega_0\tau)\}$. The three terms are centered at the frequencies $\omega = 0$, $\omega = \omega_0$ and $\omega = 2\omega_0$, respectively.

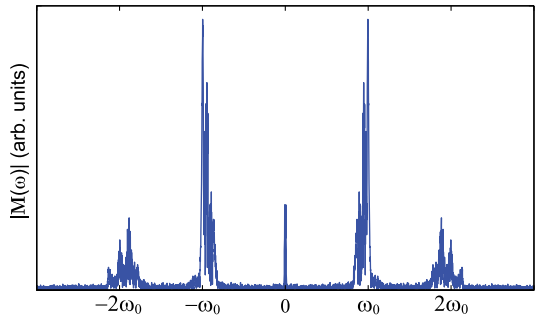

Fig. 4. (Color online) Fourier transform of the coincidence rate $M(\tau)$ in Fig. 3(a) demonstrating the spectral separation of the different terms in Eq. (3).

The background terms in Eq. (3) affect the signal-to-noise ratio (SNR). Therefore, for the same number of down-converted photons, the collinear configuration yields a lower SNR than traditional QOCT. However, the collinear configuration renders higher count-rates, which in turn increases the SNR [9,10]. Furthermore, the collinear geometry can be implemented with a wider range of parametric downconversion sources, such as periodically poled waveguides and photonics crystal fibers.

This work has been supported by DOE (grant DE-FG02-05ER46207). D. L.-M. acknowledges support from Consejo Nacional de Ciencia y Tecnología and from the Tecnológico de Monterrey (grant CAT141).

References

1. A. F. Abouraddy, M. B. Nasr, B. E. A. Saleh, A. V. Sergienko, and M. C. Teich, Phys. Rev. A **65**, 053817 (2002).
2. M. B. Nasr, B. E. A. Saleh, A. V. Sergienko, and M. C. Teich, Phys. Rev. Lett. **91**, 083601 (2003).
3. M. B. Nasr, B. E. A. Saleh, A. V. Sergienko, and M. C. Teich, Opt. Express **12**, 1353 (2004).
4. M. B. Nasr, D. P. Goode, N. Nguyen, G. Rong, L. Yang, B. M. Reinhard, B. E. A. Saleh, and M. C. Teich, Opt. Commun. **282**, 1154 (2009).
5. M. C. Booth, B. E. A. Saleh, and M. C. Teich, Opt. Commun. **284**, 2542 (2011).
6. B. I. Erkmen and J. H. Shapiro, Phys. Rev. A **74**, 041601(R) (2006).
7. M.C. Teich, B. E. A. Saleh, F. N. C. Wong, and J. H. Shapiro, Quantum Inf. Process. **10**, 1 (2011).
8. D. Lopez-Mago and L. Novotny, Phys. Rev. A **86**, 023820 (2012).
9. A. Ling, A. Lamas-Linares, and C. Kurtsiefer, Phys. Rev. A **77**, 043834 (2008).
10. M. W. Mitchell, Phys. Rev. A **79**, 043835 (2009).